Ferruginous oceans during OAE1a and collapse of the marine sulfate pool

Kohen W. Bauer[1,2,5], Cinzia Bottini[3], Sergei Katsev[4], Mark Jellinek[1], Roger Francois[1], Elisabetta Erba[3], Sean A. Crowe[1,2,5,6†]

[1]Department of Earth, Ocean and Atmospheric Sciences,
The University of British Columbia, 2020 - 2207 Main Mall,
Vancouver, British Columbia V6T 1Z4, Canada

[2]Department of Microbiology and Immunology, Life Sciences Centre,
The University of British Columbia, 2350 Health Sciences Mall,
Vancouver, British Columbia, V6T 1Z3, Canada

[3]Department of Earth Sciences,
University of Milan, Via Mangiagalli 34,
20133 Milan, Italy

[4]Large Lakes Observatory and Department of Physics
University of Duluth, 2205 E 5th St,
Duluth, Minnesota, 55812, USA

[5]Department of Earth Science
The University of Hong Kong
James Lee Building, Pokfulam Road, Hong Kong SAR

[6]The Swire Institute of Marine Science, The University of Hong Kong, Cape d'Aguilar Road, Shek O, Hong Kong SAR

[†]Corresponding author; sean.crowe@ubc.ca

Highlights

- Fe-speciation and redox sensitive trace element enrichment patterns in sediments from OAE1a (~120 Ma) reveal deposition under anoxic, ferruginous conditions in both the paleo-Tethys and paleo-Pacific oceans

- Widespread ferruginous ocean conditions during OAE1a are only possible with low seawater sulfate concentrations, which must have dropped well below 300 µM, and possibly below 100 µM.

- Mass balance of the sulfur cycle predicts that biomass associated organic S (bio-sulfur) may have played an important role as a global S-sink during OAE1a.

Abstract

Seawater sulfate is one of the largest oxidant pools at Earth's surface today and its concentration in the oceans is generally assumed to have varied between 5 and 28 mM since the early Phanerozoic Eon. Intermittent and potentially global Oceanic Anoxic Events (OAEs) are accompanied by changes in seawater sulfate concentrations and signal perturbations in the Earth system associated with major climatic anomalies and biological crises. Ferruginous (Fe-rich) ocean conditions developed transiently during multiple OAEs, implying strong variability in seawater chemistry and global biogeochemical cycles. The precise evolution of seawater sulfate concentrations during OAEs, however, is uncertain and thus models that aim to mechanistically link oceanic anoxia to broad-scale disruptions in the Earth system remain equivocal. Here, we use analyses of Fe-speciation and redox sensitive trace metals in slope sediments deposited in the Tethys and Pacific oceans to constrain seawater sulfate concentrations and underlying dynamics in marine chemistry during OAE1a, ~120 Ma. We find that large parts of the global oceans were anoxic and ferruginous for more than 1 million years. Calculations show that the development of ferruginous conditions requires that seawater sulfate concentrations drop below 300 µM and possibly below 100 µM, which is an order of magnitude lower than previous minimum estimates. Such a collapse of the seawater sulfate pool over a time scale of only one-hundred thousand years is a key and previously unrecognized feature of Phanerozoic Earth surface redox budgets. Critically, this unprecedented sensitivity has potential to dramatically alter global biogeochemical cycles, marine biology, and climate on remarkably short timescales.

1.0 Introduction

Seawater chemistry is generally thought to have evolved to its current well-oxygenated, sulfate-rich state between 540 and 420 million years ago (Ma) (Stolper and Keller, 2018). Throughout much of the preceding 3.5 billion years, the oceans were largely anoxic, predominantly Fe-rich (ferruginous), and punctuated by intervals of widespread hydrogen sulfide-rich conditions (euxinic) (Poulton and Canfield, 2011). These conditions waned in the early Phanerozoic, and thus, for much of the last 500 Myrs, marine and global biogeochemical cycles were thought to have operated much as they do today. Widespread oceanic anoxia, however, re-emerged intermittently in the Phanerozoic Eon and was particularly prevalent during warm periods such as the Cretaceous (Jenkyns, 2010). The oceans developed euxinia during some of these Oceanic Anoxic Events (OAEs) (Marz et al., 2008; Poulton et al., 2015) when pelagic microbial respiration was channelled through sulfate reduction producing hydrogen sulfide (H_2S) that accumulated in poorly ventilated water masses. Emerging evidence, however, also suggests that ferruginous conditions developed during several OAEs (OAE2, OAE3) (Marz et al., 2008; Poulton et al., 2015). Since development of ferruginous conditions hinges on the balance between Fe- and S-delivery and removal from the oceans, temporal shifts between euxinic and ferruginous conditions imply large-scale variability in ocean chemistry and the S-cycle.

The sulfur isotope record and analyses of fluid inclusions from the Cretaceous Period reveal that background seawater sulfate concentrations were much lower (3-10 mM) than the modern oceans (28 mM) (Gomes et al., 2016; Mills et al., 2017; Timofeeff et al., 2006). Episodic evaporite deposition drew seawater sulfate concentrations down even further, possibly to as low as 1 mM, during the Early Cretaceous (Wortmann and Chernyavsky, 2007) and this evaporite deposition likely took place intermittently both before (Davison, 2007), and after (Chaboureau et al., 2013), Aptian OAE1a (~120 Ma). Whereas some stratigraphic reconstructions imply evaporite deposition contemporaneous with OAE1a (Tedeschi et al., 2017), this timing is not well supported by independent chronostratigraphic data. Regardless, low seawater sulfate concentrations in the

Aptian oceans could have strongly influenced global biogeochemical cycling across the OAE1a interval. For example, seawater sulfate concentrations are an important control on marine methane (CH_4) budgets, with super-millimolar sulfate concentrations attenuating the release of CH_4 from modern marine sediments to the atmosphere through microbial anaerobic methane oxidation (Reeburgh, 2007). Sub-millimolar sulfate concentrations, in contrast, can lead to large-scale oceanic CH_4 efflux with corresponding implications for climate (Olson et al., 2016).

Paleomarine sulfate concentrations have mostly been estimated through two approaches; 1) the rate method, and 2) the microbial sulfate reduction (MSR) trend method (e.g., Algeo et al. (2015), Supplementary Information), but these, importantly, do not resolve seawater sulfate concentrations below about 1 mM. The rate and MSR methods are based on the magnitude of S-isotope fractionation between cogenetic sulfate and sulfide ($\Delta^{34}S_{CAS\text{-}Pyrite}$), the rate of change in seawater sulfate $\delta^{34}S$ (based on $\delta^{34}S$ in carbonate associated sulfate (CAS) or barite minerals), empirical relationships between $\Delta^{34}S_{CAS\text{-}Pyrite}$, and sulfate concentrations calibrated in modern environments (Algeo et al., 2015). When applied to the early Aptian oceans using existing S-isotope data (Gomes et al., 2016; Kristall et al., 2018; Mills et al., 2017), these methods yield estimates for seawater sulfate that are less than 1-3 mM (Fig. 1). There are, however, critical limitations to these estimates. For example, the rate method only provides maximum estimates for seawater sulfate concentrations because the measured rate of change in $\delta^{34}S_{Seawater}$ in a given sedimentary unit is generally smaller than the calculated theoretical maximum, which is mathematically obtained when the source flux of sulfate to the oceans is zero (Algeo et al., 2015) (Supplementary Information) (Fig. 1). Since this scenario does not occur in nature, estimates provided by the rate method tend to be larger than actual seawater sulfate concentrations (Algeo et al., 2015). On the other hand, while there is a relationship between sulfate concentrations and the magnitude of S-isotope fractionations (Algeo et al., 2015), the controls on microbial sulfate reduction and associated isotope fractionation are complex and incompletely known (Canfield and Farquhar, 2012), confounding precise application of the MSR method to the geologic record.

Both methods are thus incapable of resolving seawater sulfate concentrations across the Aptian beyond coarse maximum estimates of 1-3 mM (Fig. 1). The sensitivity of biogeochemical cycles below this range, however, is important and highlights the need for new data and models that provide more accurate and precise reconstructions of seawater sulfate concentrations during the Aptian Age.

Recognizing the limitations of the rate and MSR methods, we took a different approach to reconstructing seawater sulfate concentrations in the Aptian oceans. We studied sedimentary rocks from the Tethys (Cismon drill core) and Pacific (Deep Sea Drilling Project (DSDP) Site 463) oceans that capture OAE1a (Fig. S1). OAE1a is delineated by organic matter (OM)-rich black shale containing units that were deposited over more than a million years (Erba et al., 2010; Malinverno et al., 2010). We conducted a suite of geochemical and mineralogical analyses, which collectively reveal that OAE1a sediments were deposited under anoxic Fe-rich (ferruginous) water column conditions that extended from the Tethys to the Pacific oceans and persisted for more than 1 million years. Our modeling reveals that development of these ferruginous conditions was a response to collapse of the seawater sulfate pool associated with expanded oceanic anoxia.

2.0 Methods

2.1 Sediment digestions and Fe-speciation analyses

We took care to work with well-preserved sedimentary rock samples from both the Cismon and DSDP Site 463 drill cores. These rocks were powdered first using an agate mill and then by hand using an agate mortar and pestle. Sample splits (200 mg) were entirely digested in a lithium metaborate fusion, using a sample to LiO_2 flux ratio of 1:1. Sample splits of 500 mg of sediment were subjected to the Fe-speciation sequential extraction scheme (Poulton and Canfield, 2005). We also performed a revised extraction scheme that included an organic matter leach, as indicated in (Table S1). For the revised scheme our "highly reactive, Fe_{HR}" pool is defined as carbonate-associated Fe ($Fe_{carb,}$ 0.5 N HCl extractable Fe), organic matter associated Fe (Fe_{OM}), ferric (oxyhydr)oxides including magnetite ($Fe_{Oxides,}$ sum of dithionite and oxalate extractable Fe, Fe_{Goe}

and $Fe_{Magnetite}$, Table S1), and pyrite (Fe_{Pyr}) (Fe_{HR} = Fe_{Carb} + Fe_{OM} + Fe_{Oxides} + Fe_{Pyr}). The Fe_{Tot} pool is the sum of all Fe_{HR} pools and Fe contained in silicate minerals (Fe_{Sil}).

2.2 Elemental concentrations

Extract Fe concentrations were measured by both flame atomic adsorption spectroscopy (Flame AAS, Varian 875) and inductively coupled optical emission mass spectroscopy (ICP-OES, Varian 725ES). Extract major and trace element concentrations were measured by quadrupole inductively coupled plasma mass spectroscopy (Q-ICP-MS, Perkin Elmer NexION 300D), while major elemental concentrations were determined by inductively coupled optical emission mass spectroscopy (ICP-OES, Varian 725ES). For flame AAS measurements, precision on triplicate measurements was 1.2% (1 RSD) and our limit of detection in solution was 80 μg L^{-1}, or roughly 35 μg g^{-1} sediment Fe, based on dilutions. For our ICP-OES measurements precision on triplicate measurements for Fe was 2.2% (1 RSD) and our limit of detection in solution was 6 μg L^{-1}, or roughly 30 μg g^{-1} sediment, based on dilutions. For Al analysis via ICP-OES, precision on triplicate measurements was 1.2% (1 RSD) and our limit of detection in solution was 6 μg L^{-1}, or roughly 33 μg g^{-1}, based on dilutions. Our extractions dissolved >92% of the Fe from the PACS-2 international reference standard. Errors on Fe concentrations in the different leachates based on triplicate extractions of the PACS-2 international reference standard are as follows (reported as 1 sigma RSD); Fe_{Aca} ± 6.0%, $Fe_{0.5NHCl}$ ± 5.8%, Fe_{Dith} ± 2.8%, Fe_{Oxa} ± 10.1%, Fe_{Sil} ± 3.4%.

For our Q-ICP-MS measurements, precision on Cr was <1% (1 RSD) and our limit of detection in solution was 0.03 μg L^{-1}, or roughly 0.7 μg g^{-1} sediment Cr, based on dilutions. For Cr analysis via ICP-OES, we achieved an RSD of <1% and our limit of detection was roughly 5.3 μg g^{-1} sediment, based on dilutions. For V analysis via ICP-OES, we achieved an RSD of <1% and our limit of detection was 0.26 μg g^{-1} sediment, based on dilutions. For U and Mo analysis via Q-ICP-MS, we achieved RSDs of <1% and 3.5% respectively, and our limits of detection were roughly 0.10 and 0.40, respectively μg g^{-1} sediment, based on dilutions. Our fusion

digestions dissolved ~100%, 97% and 100% of the Cr in the BHVO-2, MESS-3, and PACS-2 international reference standards, respectively.

2.3 Microscopy and XRD

Polished thin sections of the Cismon and DSDP Site 463 rocks were imaged on a Hitachi S-4800 field emission scanning electron microscope (Hitachi S-4800 FEG SEM) equipped with field emission gun. Elemental concentrations were used to infer mineralogy, and these were determined by energy-dispersive X-ray spectroscopy (EDS, Oxford Instruments X-Max 80 Detector) based on X-ray fluorescence at the relevant emission energies for Fe, C, S, P, Ca and O. Sediment mineralogy was determined by powder X-ray diffraction (XRD). Rock powders were mounted on non-diffracting silica plates. Continuous-scan X-ray diffraction data were collected over a range 3-90°2θ with CoKα radiation on a Rigaku Miniflex diffractometer. We analyzed the X-ray diffractograms using the International Centre for Diffraction Database PDF-4, RRUFF database, and Search-Match software by JADE. The XRD data is plotted in Figure. S2.

2.4 1D water column reactive transport model

We developed a reaction transport model to explore how surface ocean sulfate concentrations influence water column sulfate drawdown and rates of pyrite deposition. This model was developed and described in detail in Crowe et al. (2014) with additional details provided in the Supplementary Information. The model predicts seawater sulfate distributions under steady-state conditions by describing changes in sulfate concentration with depth as a function of vertical transport and rates of sulfate reduction to sulfide as:

$$K_z \frac{\partial^2[SO_4^{2-}]}{\partial x^2} - R_{SR} = 0 \qquad (1)$$

where K_z is the eddy diffusivity governing vertical mixing ($m^2\ d^{-1}$), x is the depth in the water column (m), and R_{SR} is the sulfate reduction rate ($\mu mol\ m^{-3}\ d^{-1}$). For K_z, we implemented a range of values (0.01 – 1 $m^2\ d^{-1}$), of which the highest value is

similar to globally averaged open ocean vertical transport rates (Munk and Wunsch, 1998), and with lower values representing more strongly stratified seas (Table S2). Sulfate reduction rates were calculated with a Michaelis-Menten like kinetic description:

$$R_{SR} = \frac{V_{max}[SO_4^{2-}]}{K_m + [SO_4^{2-}]} \qquad (2)$$

where K_m is the half-saturation constant (μM). For K_m, we considered a range of values from 3.6 to 450 μM, which are characteristic of organisms from modern environments with both high and low seawater sulfate concentrations (Table S2). V_{max} is the maximum rate of sulfate reduction (μmol m^{-3} d^{-1}), when sulfate supply is unlimited, and thus corresponds to the scenario when sulfate reduction is limited by organic matter availability. V_{max} can, therefore, be estimated based on models of organic matter degradation rates in modern anoxic marine systems. We thus parameterized V_{max} according to carbon degradation rates in the modern ocean under both high (V_{max} = 15 μM yr^{-1}) and low productivity (V_{max} = 1 μM yr^{-1}) scenarios (Crowe et al., 2014; Hartnett and Devol, 2003) (Table S2).

We set two conditions that tether our model reconstructions for seawater sulfate to the rock record: 1) pyrite burial fluxes were used to place tight limits on total sulfide production fluxes, which cannot be greater than the pyrite burial fluxes recorded in OAE1a sediments assuming all H_2S is quantitatively converted to pyrite; and 2) under ferruginous conditions, seawater sulfate concentrations must be quantitatively drawn down to preserve non-pyritized Fe_{HR} in the presence of abundant organic matter. Pyrite burial fluxes were calculated by combining sedimentation rates (Malinverno et al., 2010) with pyrite concentrations in the Cismon and DSDP Site 463 sediments. Together, these two conditions place upper limits on the maximum sulfate flux that can be converted to pyrite through microbial sulfate reduction and reaction of the sulfide produced with Fe_{HR}. We thus use our model to identify a parameter space of possible upper bounds for seawater sulfate concentrations.

2.5 Sulfur mass balance model

To connect the results of our reactive transport modeling to the requisite dynamics in the global sulfur cycle we developed a box model following published studies (Gomes et al., 2016; Mills et al., 2017). Through a system of coupled evolution equations, we track the mass and isotopic composition of marine sulfate as a function of sources and sinks of sulfur to and from the ocean using the following equations;

$$\frac{\partial M_s}{\partial t} = F_w + F_h - (F_{pyr} + F_{evap} + F_{OM} + F_{CAS}) \qquad (3)$$

$$\frac{\partial \delta 34\mathrm{Ssulphate}}{\partial t} = ((F_w \delta_w + F_h \delta_h) - \delta^{34}S_{Sulphate}(F_w + F_h) - F_{pyr}\Delta^{34}S\ )/M_s \qquad (4)$$

Here, M_S is the mass of sulfur in the ocean; F_H, F_W, are the hydrothermal (including volcanic), and weathering input fluxes of S, respectively; F_{pyr}, F_{OM}, F_{CAS} and F_{evap} are the burial fluxes of pyrite, biomass associated organic S (bio-sulfur), carbonate associated sulfate, and evaporites, respectively. $\delta^{34}S_{sulphate}$ is the S-isotope composition of seawater sulfate. δ_w and δ_h are the S-isotope composition of the weathering (5.2‰) and hydrothermal (3.2 ‰) inputs respectively, $\Delta^{34}S$ is the average isotope fractionation factor associated with pyrite deposition (36.0‰). To obtain an initial value for M_S, we assume an ocean volume of 1.38 x 10^{18} m^3 and an initial sulfate concentration of 4 mM, in accordance with Cretaceous estimates based on the chemical composition of fluid inclusions and like previous modeling work (Gomes et al., 2016; Timofeeff et al., 2006; Wortmann and Chernyavsky, 2007). We take $\delta^{34}S_{sulphate}$ = 19.5‰ as an initial value, which is within error of measurements of pre-OAE1a $\delta^{34}S_{CAS}$. From these initial conditions, we establish a pre-OAE1a steady-state condition (Table S4). Additional details can be found in the Supplementary Information.

3.0 Results

3.1 Fe-speciation

Fe-speciation analyses reveal enrichments of pyritizable Fe (Fe_{HR}) across the OM-rich shale intervals that define OAE1a in both Cismon and DSDP Site 463 rocks (Fig. 2), relative to rocks stratigraphically above and below. Ratios of Fe_{HR}/Fe_{Tot} >0.38 imply sediment deposition beneath anoxic waters if ratios of Fe_{Tot}/Al are also >0.5 and C_{org} contents are >0.5 wt% (Raiswell et al., 2018). Fe_{HR}/Fe_{Tot} values recorded in the Cismon core during OAE1a are consistently above 0.38 and have Fe_{Tot}/Al >0.5 as well as C_{org} >0.5 wt%, diagnostic of deposition below an anoxic water column (Fig. 3). Fe_{HR}/Fe_{Tot} ratios in rocks that bound OAE1a have Fe_{HR}/Fe_{Tot} <0.38) (Fig. 3). Similarly, Fe_{HR}/Fe_{Tot} ratios in rocks deposited at DSDP Site 463 also capture intervals with values >0.38 and Fe/Al >0.5 and C_{org} >0.5 wt%. However, some Fe_{HR}/Fe_{Tot} values in sediments deposited during OAE1a at DSDP Site 463, are below the Fe_{HR}/Fe_{Tot}>0.38 threshold (Fig. 3). The sediments deposited during OAE1a, at both sites studied, also preserve appreciable non-pyritized Fe_{HR} (Fig. 2). Fe_{Pyr}/Fe_{HR} ratios are a direct measure of the degree of pyritization of the highly reactive Fe_{HR} pool and ratios <0.7 indicate deposition under a ferruginous water column with excess highly reactive Fe (Raiswell et al., 2018). All rocks deposited at the Cismon and DSDP 463 sites during the OAE1a interval have Fe_{Pyr}/Fe_{HR} <0.7 (Fig. 3).

The 0.5 N HCl leach selectively dissolves poorly crystalline Fe (oxyhydr)-oxides, reactive Fe-carbonates, and acid volatile sulfide (AVS). Determination of both Fe(II) and Fe(III) in the 0.5 N HCl leach, therefore, provides a means of further speciating Fe between highly reactive Fe(II) and Fe(III) phases, as well as determining the association of other elements, like P, with these phases. We find that there was detectable Fe(III) in most of the 0.5 N HCl extracts (Fig. S3), but that this Fe(III) represented a very small component of the total highly reactive Fe in the sediments. For Cismon sediments this translates to an average of ~0.5% of the Fe_{HR} pool. For DSDP Site 463 sediments this translates to an average of ~2.0% of the Fe_{HR} pool (Fig. S3). Furthermore, we observe that on average only 7% and 5% of the total P is associated with poorly crystalline Fe-(oxyhydr)-oxide phases in the Cismon and DSDP Site 463 sediments, respectively (Fig. S3).

383 *3.2 Redox sensitive trace elements (RSTEs)*

384 Multiple redox sensitive trace elements (RSTEs) display strong enrichments
385 relative to the Post Archean Average Shale (PAAS) reference material (McLennan,
386 2001). Rhenium is highly enriched in OAE1a sediments (Fig. 4), with average Re
387 concentrations of 100 and 2.0 ng g^{-1} in the Cismon and DSDP Site 463 cores,
388 respectively. Average Re concentrations in rocks that bound OAE1a are 1.0 and
389 1.0 ng g^{-1} in the Cismon and DSDP Site 463 cores, respectively (Fig. 3). During
390 OAE1a average shale normalized Re enrichment factors (Re_{EF}) are 746 and 18 in
391 the Cismon and DSDP Site 463 cores, respectively. Average Re_{EF} in rocks that
392 bound OAE1a are 15 and 21 in the Cismon and DSDP Site 463 cores, respectively
393 (Fig. 4). During OAE1a Cr enrichment factors (Cr_{EF}) are 5.0 and 4.0 in the Cismon
394 and DSDP Site 463 cores, respectively. Average Cr_{EF} in rocks that bound OAE1a
395 are 3.9 and 1.1 in the Cismon and DSDP Site 463 cores, respectively (Fig. 4).
396 During OAE1a average V enrichment factors (V_{EF}) are 2.5 and 1.7 in the Cismon
397 and DSDP Site 463 cores, respectively. Average V_{EF} in rocks that bound OAE1a
398 are 1.1 and 1.3 in the Cismon and DSDP Site 463 cores, respectively (Fig. 4). In
399 addition to our new RSTE data, and in contrast to Re, V, and Cr, a compilation of
400 Mo concentrations in sediments deposited across OAE1a (Charbonnier et al.,
401 2018; Follmi, 2012; Westermann et al., 2013) shows that only 2 out of 196 samples
402 analysed have Mo concentrations greater than the 25 µg g^{-1}, a threshold that
403 implies deposition under euxinic conditions (Lyons and Severmann, 2006) (Fig.
404 4e).

405

406 *3.3 Microscopy and XRD*

407 In both the Cismon and DSDP Site 463 sediments, the presence of Fe_{HR} is
408 demonstrable through X-ray diffraction analyses (Fig. S2). An appreciable fraction
409 of this Fe_{HR} is preserved as Fe_{Carb} (Supplementary Data), which operationally
410 reflects the mineral siderite (Fig. S2). In thin section, pyrite crystals in the Cismon
411 and DSDP Site 463 rocks are well-preserved, lacking evidence of oxidation rims,
412 dissolution pitting, or pervasive cracking (Fig. 5). A collection of images of
413 consistently well-preserved pyrite (including framboids) from multiple thin sections

414 are broadly representative of the OAE1a sediments (Fig. 5). Additionally, electron
415 micrographs and corresponding SEM-EDS analyses reveal pristine Ca-P-rich
416 minerals (apatite) and demonstrate a much stronger association of P with Ca than
417 Fe (Fig. 5).
418
419 *3.4 1D water column reaction transport modeling*
420 Results from the water-column reactive transport modeling illustrate how
421 sulfate drawdown and pyrite burial fluxes scale as a function of surface ocean
422 sulfate concentrations. These calculations yield estimates for seawater sulfate that
423 must be less than ~300 µM, and less than 100 µM under most scenarios (Fig. 6).
424 A sensitivity analysis of our model and its relevant parameters (V_{max}, K_m and K_z)
425 provides constraints on allowable seawater sulfate concentrations that fulfill
426 conditions that sulfate concentrations be drawn down to negligible values
427 (condition 1, Methods section 3.4) without exceeding the pyrite/S-burial rates
428 recorded in the OAE1a sediments (condition 2, Methods section 3.4). Higher
429 values of K_m result in lower rates of sulfate reduction and pyrite burial. Higher
430 values for V_{max} result in high rates of sulfate reduction and pyrite burial. The K_z
431 values used are conservative with respect to sulfate concentrations as higher
432 values for K_z lead to lower possible surface seawater sulfate concentrations (Fig.
433 6) (Table S2). In general, the scenario which leads to the maximum predicted
434 seawater sulfate concentration (~300 µM) corresponds to V_{max} values similar to
435 respiration rates in modern anoxic water columns (~7 µM yr^{-1}), high K_m (450 µM),
436 and slightly more sluggish vertical mixing (K_z, 0.1 m^{-2} d^{-1}) relative to the modern
437 open oceans (Fig. 6) (Table S2). All other scenarios that satisfy model conditions
438 1 and 2 (Section 2.4) yield lower seawater sulfate concentrations.
439
440 *3.5 Sulfur mass-balance model*
441 Global sulfur mass balance modeling reveals that low µM seawater sulfate
442 concentrations during OAE1a are supported by existing constraints on global S-
443 budgets and S-isotope data. A perturbation to the global S-cycle lasting roughly
444 0.5 Myrs led to enhanced hydrothermal and riverine S-inputs (Mills et al., 2017) of

~2.3 ± 0.6 Tmol yr^{-1} and ~3.1 ± 0.8 Tmol yr^{-1}, respectively (Fig. 8), assuming a conservative ~25% uncertainty for the different S-fluxes (Canfield and Farquhar, 2012). To both balance enhanced S-inputs and draw seawater sulfate down to concentrations that satisfy the 1D modeling results (Fig. 6), requires S-burial fluxes of 5.4 ± 1.7 Tmol yr^{-1} (95% confidence interval, Fig. 8). The Aptian S-isotope record, furthermore, is satisfied, within the uncertainties of Cretaceous S-fluxes (Table S4), when oceanic S-removal fluxes are appropriately distributed between pathways that are strongly isotopically fractionated from seawater (i.e., pyrite), and those that are not (i.e., CAS, barite, and bio-sulfur, Fig. 8). Following OAE1a, the seawater sulfate pool can rebound to mM sulfate concentrations on timescales of ~1 Myrs through a reduction in S-removal fluxes and the continued supply of S through volcanism and weathering that is largely unchanged over this time scale (Jellinek et al., 2020) (Fig. 8).

4.0 Discussion

4.1 Sample fidelity

The OAE1a rocks we analyzed from both Cismon and DSDP 463 appear pristine with little evidence for post-depositional oxidation. Previous work observed extensive pyrite oxidation during storage of OAE sediments (OAE2, Kraal et al., 2009). We thus assessed potential post-depositional oxidation through detailed optical and electron microscopy, focusing on observations of pyrite crystal morphology and texture along cracks, or near sample edges where pyrite grains are most exposed to the atmosphere. Visually, all pyrite grains observed in both cores appear well-preserved (Fig. 5) with no evidence of post-depositional oxidation. We also observe pristine Ca-P-rich minerals and limited association of P with Fe (Fig. 5). Pyrite oxidation can cause dissolution of Ca-P minerals and a redistribution of P into newly formed Fe-(oxyhydr)oxide minerals (Kraal et al., 2009). Thus, the preservation of Ca-P-rich minerals in our samples and lack of Fe-associated P further implies negligible oxidation artifacts (Supplementary Information).

Tests for more subtle effects of post depositional alteration based on geochemical information support microscopic observations and demonstrate negligible oxidation of sediment Fe-species. Key Fe- and S-bearing minerals sensitive to oxidation include acid volatile S-minerals (AVS), pyrite, and/or siderite. Recognizing that the initial product of acid volatile S (AVS), pyrite, and/or siderite oxidation is poorly crystalline Fe (oxyhydr)-oxides (Luther III et al., 1982), such oxidation would be observed as 0.5 N HCl leachable Fe(III). Most Fe leached in 0.5 N HCl was Fe(II) and the concentration of 0.5 N HCl leachable Fe(III) in all rocks analyzed was a negligible (<2%) component of the total Fe_{HR} (Fig. S3). Importantly, 0.5 N HCl leachable Fe(III) is not expected to be preserved in anoxic, OM-rich sediments, and the Fe(III) we measured in this fraction may thus be the product of very limited post depositional oxidation. Critically, however, such a small amount of post depositional oxidation has a negligible effect on our Fe-speciation results and their interpretation (Fig. S4), as we show in detail below.

The conversion of both pyrite and siderite to Fe (oxyhydr)-oxides during sample oxidation can cause a redistribution of Fe from Fe_{Pyr} and Fe_{Carb} to Fe_{Ox}. Because these pools are summed in the Fe_{HR} pool, oxidation has little potential to influence the Fe_{HR}/Fe_{Tot} or Fe/Al ratios, that are used to discriminate between oxic versus anoxic conditions. However, Fe-speciation discriminates between ferruginous and euxinic conditions based on $Fe_{Pyr}/Fe_{HR,}$ with ferruginous conditions indicated at conservative ratios <0.7. Given that pyrite oxidation decreases this ratio, it has potential to obscure signals for euxinia. We thus tested our capacity to accurately discriminate between ferruginous and euxinic conditions based on Fe_{Pyr}/Fe_{HR} ratios measured in our samples by fully unpacking the wealth of information in Fe-speciation analyses (Fig. S4). As one example, we summed Fe_{Ox}, the product of Fe_{Pyr} oxidation, with Fe_{Pyr} to come up with a maximum possible 'pre-oxidation' ratio, Fe'_{Pyr}/Fe_{HR}. Fe'_{Pyr}/Fe_{HR} ratios in both the Cismon and DSDP Site 463 sediments are nearly all below the conservative <0.7 threshold for the delineation of ferruginous conditions (Fig. 3). As a further example, we assumed all the sulfur present in the sediment was originally pyrite and calculate conservative pyritized Fe values (S_{Tot}/Fe_{HR}). We find that these values are also

below the conservative threshold of 0.7 in both the Cismon and DSDP Site 463 sediments (Fig. S4). We employed an additional 3 tests (Supplementary Information) and together these all demonstrate that our Fe-speciation analyses are robust, and that sample oxidation had negligible, if any, effect on our ability to discriminate between euxinic and ferruginous conditions (Fig. S4).

4.2 Anoxic ferruginous conditions

Fe-speciation in sediments deposited at both the Cismon and DSDP Site 463 sites records deposition under anoxic, ferruginous water column conditions (Fig. 3). Ratios of Fe_{HR}/Fe_{Tot} >0.38 in all the Cismon sediments deposited during OAE1a are diagnostic of anoxic conditions in the Tethys Ocean. Some Fe_{HR}/Fe_{Tot} values in sediments deposited during OAE1a at DSDP Site 463, however, are below the threshold (>0.38) used to diagnose anoxia and are thus ambiguous to depositional redox state based on Fe-speciation alone. We note, however, that Fe-speciation analyses cannot diagnose sediment deposition under oxic conditions. This is because of Fe mass-balance, which dictates that enrichment of Fe_{HR} at one depositional location by necessity requires its depletion in another. Some sediments must, therefore, act as a source of Fe_{HR}. It follows that Fe_{HR}/Fe_{Tot} ratios <0.38 can also result from deposition beneath an anoxic water column and such ratios signify that the strength of the Fe-shuttle, and Fe-delivery to the open Pacific Ocean (DSDP Site 463), likely waxed and waned throughout OAE1a. In contrast, continental slope sediments, like those deposited at the Tethys site (Cismon core), likely served as more persistent and effective oceanic sinks for Fe_{HR}. Sediments deposited during OAE1a at both sites preserve appreciable non-pyritized Fe_{HR}, which thus signals deposition and burial in a sulfide poor, ferruginous setting. Values <0.7 are due to preservation of non-pyritized Fe_{HR} and, by definition, such values require insufficient sulfide supply to pyritize the available Fe_{HR}, and this thus also precludes accumulation of free sulfide and the development of euxinia. Values of Fe_{Pyr}/Fe_{HR} <0.7 preserved in sediments deposited under anoxic conditions (Fe_{HR}/Fe_{Tot} >0.38), therefore, either reflect sulfate depletion and deposition from a

sulfate and sulfide poor water column, or lack of sulfide production from available sulfate, which we revisit below.

The distribution of RSTEs in sediments from both the Cismon and DSDP 463 sites also reveals deposition under anoxic, ferruginous conditions. Rhenium is highly enriched in OAE1a sediments, and this confirms deposition under anoxic conditions at both sites given tendency for Re enrichment under both ferruginous, and to a lesser degree euxinic conditions (Tribovillard et al., 2006) (Fig. 3). Deposition under euxinic conditions is often accompanied by strong Mo enrichments and deposition under euxinic conditions can be conditionally inferred when sedimentary Mo concentrations are >25 μg g^{-1} (Lyons and Severmann, 2006). However, most OAE1a samples analysed here have a conspicuous lack of Mo enrichment with correspondingly strong enrichments in other RSTEs (V, Cr, Re) (Fig. 4). This supports the Fe-speciation data and diagnoses the deposition of sediments at the Cismon and DSDP 463 sites under ferruginous, rather than euxinic conditions.

Our conclusion for deposition of OAE1a sediments under ferruginous conditions is underscored by comparisons of RSTE distributions in OAE1a sediments and those deposited in euxinic regions in the modern oceans. Strikingly, the general pattern of RSTE enrichments (Cr, V, Re) with lack of corresponding Mo enrichment in the OAE1a sediments, strongly contrasts observations from modern euxinic sediments (Bennett and Canfield, 2020) (Fig. 7). This can be seen when enrichment factors (EF) of these RSTEs are normalized to Mo_{EF} in the OAE1a sediments and compared to ratios of $RSTE_{EF}/Mo_{EF}$ in example modern euxinic basins (Fig. 7). Most strikingly, Cr, V, and Re are on average 150, 50, and 10 times more enriched in the OAE1a sediments than in modern euxinic sediments, relative to Mo, respectively (Fig. 7). Furthermore, concentrations of Mo >25 μg g^{-1}, sporadically observed in some OAE1a sediments from other sites (Fig. 4e), need not reflect deposition from euxinic waters. Instead, such enrichments can be achieved through a variety of processes and given the Fe-speciation and OM contents of OAE1a sediments, likely reflect Fe-oxide and OM-Mo shuttling to the sediment (Hardisty et al., 2018). We note that development of global euxinia

for a brief interval at the initiation of OAE1a, and/or hydrological restriction and reservoir effects, have potential to induce widespread drawdown in seawater RSTE inventories (Tribovillard et al., 2006), possibly contributing to muted Mo_{EF}. Such drawdown, however, doesn't explain the broader pattern of RSTE distributions given that several non-Mo RSTEs are strongly enriched. Instead, the RSTE enrichment patterns of OAE1a sediments must reflect pervasive anoxic conditions throughout OAE1a and given known mechanisms for differential RSTE enrichments, and our Fe-speciation results, the enrichments in Cr, V, and Re are best explained by deposition from ferruginous oceans.

4.3 Surface-ocean sulfate scarcity during OAE1a

In organic matter (OM)-rich settings, like those that supported deposition of OAE1a sediments, residual sulfate is incompatible with Fe_{Pyr}/Fe_{HR} <0.7. This is because under anoxic conditions, available OM supports sulfate reduction and corresponding sulfide production until either sulfate or OM is exhausted. Fe_{Pyr}/Fe_{HR} <0.7 can develop in scenarios where there is insufficient OM to fuel sulfate reduction, as is the case in many modern hydrothermal sediments (e.g., Southeast Pacific Rise (SEPR)), which are different than the sediments deposited during OAE1a. The two scenarios can be easily distinguished by both the sediment OM content (e.g., OAE1a >8 wt%, SEPR <0.01 wt%), and by the speciation of non-pyritized Fe_{HR}. Appreciable OM tends to fuel reduction of Fe_{HR} and conversion of ferric (oxyhydr)-oxide phases to minerals like siderite and magnetite, whereas lack of OM tends to preserve ferric (oxyhydr)-oxides as minerals like goethite or hematite, as in the goethite dominated sediments of the SEPR (Poulton and Canfield, 2006). Sulfate reduction and resulting pyritization of Fe_{HR} during deposition of OAE1a sediments was, therefore, not OM-limited, and instead must have been sulfate limited. This conclusion is underscored by the appreciable fraction of Fe_{HR} preserved as Fe_{Carb} (Supplementary Data), which operationally reflects the mineral siderite, the presence of which was also unambiguously demonstrated through X-ray diffraction analyses (Fig. S2). Notably, the preservation of siderite also requires depletion of sulfate since siderite is rapidly

598 ($t_{1/2}$ = 22 minutes) converted to pyrite when exposed to sulfide (Berner, 1981;
599 McAnena, 2011). All rocks deposited at the Cismon and DSDP 463 sites during
600 the OAE1a interval have Fe_{Pyr}/Fe_{HR} <0.7, and host appreciable $Fe(II)_{HR}$ phases.
601 The concurrent preservation of abundant sedimentary OM and non-pyritized
602 $Fe(II)_{HR}$ thus demonstrates that pyritization was limited by sulfate availability and
603 implies sulfate drawdown to negligible concentrations.
604 Surface ocean seawater sulfate concentrations were below 300 µM and
605 potentially less than 100 µM during the deposition of OAE1a sediments. Using
606 rates of microbial sulfate reduction and physical transport parameterized based on
607 modern marine organisms and ecosystems (Table S2), 1D water-column modeling
608 across scenarios that capture the entire possible parameter space yields estimates
609 for seawater sulfate that were less than ~300 µM in all scenarios, and less than
610 100 µM under most reasonable scenarios (Fig. 6). Importantly, imposing higher
611 sulfate concentrations in this model with realistic transport across oceanic
612 pycnoclines and sediment accumulation rates, yields pyrite burial fluxes much
613 higher than those recorded in OAE1a sediments (conservative maximum = 10
614 mmol m^{-2} yr^{-1}) (Fig. 6). Other parameter values at higher sulfate concentrations
615 and appropriately low pyrite burial rates leave residual sulfate in the water column
616 and are thus incompatible with the preservation of non-pyritized $Fe(II)_{HR}$, in OM-
617 rich sediments, and sediment deposition under ferruginous conditions (Fig. 6).
618
619 *4.4 Seawater sulfate dynamics in the Aptian age*
620 Our observation of ferruginous conditions during OAE1a requires a decline
621 of the seawater sulfate pool from low mM to hundreds of µM concentrations over
622 an interval on the order of 50 kyrs, commensurate with the rapid onset of
623 ferruginous conditions during OAE1a, as delineated by the Fe-speciation and C-
624 isotope records (Fig. 2). Seawater sulfate concentrations were drawn down to as
625 low as 1 mM preceding OAE1a as the result of evaporite deposition (Wortmann
626 and Chernyavsky, 2007). Evaporite deposition effectively draws sulfate down to 1
627 mM, but when sulfate concentrations drop below 1 mM, seawater saturation with
628 respect to sulfate-minerals (gypsum) during evaporation requires unrealistically

high Ca^{2+} concentrations that are inconsistent with Aptian seawater chemistry (Timofeeff et al., 2006) (Fig. S5). Our observation of ferruginous conditions and sub-mM surface ocean seawater sulfate concentrations thus effectively rule out the deposition of OM-rich shales at the same time as the formation of evaporites containing abundant gypsum. This requires that evaporitic gypsum deposition likely took place before the OAE1a interval, in the Late Barremian to early Aptian, as previously considered (Davison, 2007). Seawater sulfate drawdown to <300 µM, instead, requires a second phase of sulfate sequestration through microbial sulfate reduction and pyrite deposition and burial. Expansion of the pyrite S-sink during OAE1a provides a plausible mechanism to lower seawater sulfate concentrations and drive subsequent development of ferruginous conditions.

Enhanced pyrite burial associated with expansion of oceanic anoxia offsets strong hydrothermal and weathering inputs of S to the oceans during OAE1a and contributes to sulfate drawdown. Sulfur mass balance modeling reveals that an increase in global pyrite deposition rates from 0.66 to a maximum of 2.5 ± 0.6 Tmol yr^{-1} (Fig. 8), partly offsets enhanced S-inputs and contributes to sulfate drawdown, while remaining consistent with the S-isotope record (Fig. 8). We note that pyrite deposition rates are higher under anoxic conditions and indeed pyrite burial rates are elevated by up to a factor of ~10 during OAE1a (Fig. 2). Such enhanced pyrite burial could be achieved by expanding the global extent of water column anoxia. For example, if water column anoxia expanded from 0.1%, its extent in the modern ocean (Martin et al., 1987), to up to ~10%, the increase from 0.66 to 2.5 ± 0.6 Tmol yr^{-1} could be achieved with area specific pyrite deposition rates of 0.07 ± 0.02 mol S m^{-2} yr^{-1} in regions of ocean anoxia, which is similar to rates of pyrite burial in sediments underlying modern OMZs (Fig. S6). While enhanced pyrite burial during OAE1a can remove some S (Fig. 8), the potentially strong input fluxes from hydrothermalism and weathering require an additional S-sink to draw seawater sulfate concentrations down to levels that support ferruginous conditions.

Bio-sulfur is an additional, yet often overlooked, sulfur sink that when combined with pyrite burial, is sufficiently large to draw seawater sulfate down to <300 µM. Sinks such as bio-sulfur, CAS, or barite associated with OM, are all

known to operate in low sulfate modern and ancient environments (Horner et al., 2017; Paris et al., 2014). While bio-sulfur is a major pathway for S burial in lacustrine environments, it is often neglected in the marine S cycle. Marine organisms have molar C/S ratios between ~30 and ~50 (Chen et al., 1996; Fagerbakke et al., 1996), and thus the burial flux of organic S is likely on the order of 5 to 10 wt% that of organic C. Marine organisms, furthermore, assimilate S with a $\delta^{34}S$ composition nearly identical to seawater (Werne et al., 2003), and indeed, OAE1a S-isotope mass balance requires non-pyrite sinks that carry near seawater $\delta^{34}S$ values (Fig. 8). Given the total S and OM contents of the Cismon sediments deposited during OAE1a (Bottini et al., 2012), and assuming all non-pyrite S is buried as bio-sulfur, we calculate C:S molar ratios between 5 and 49 (average of 24), revealing that OM buried during OAE1a has a similar C:S composition to that of modern bio-sulfur. OM burial during OAE1a increased by an average factor of ~10 (range = 1 – 40x) at the Cismon and DSDP 463 sites (Fig. 2). If this OM was ~5 wt% S, a conservative 10-fold increase in OM burial during OAE1a (~3.5 ± 0.9 Tmol S yr^{-1}) would be, together with pyrite burial (2.5 ± 0.6 Tmol S yr-1), sufficient to draw the marine sulfate reservoir down to 550 ± 290 µM during OAE1a (Fig. 8), within error of estimates from our 1D model (Fig. 6).

Although uncertainties in Cretaceous S-budgets and fluxes are large, our modeling estimates plausible seawater sulfate concentrations within available constraints. Importantly, our model results reproduce $\delta^{34}S_{CAS}$ records and S burial fluxes in OAE1a sediments at seawater sulfate concentrations that are consistent with ferruginous conditions. The development of ferruginous conditions can, therefore, be attributed to widespread oceanic anoxia and ensuing sulfate drawdown through pelagic sulfate reduction and enhanced burial of bio-sulfur, all against the backdrop of low Cretaceous seawater sulfate concentrations, strong hydrothermalism, and weathering. Furthermore, at a seawater sulfate concentration of ~250 µM and peak S-fluxes in our mass balance model, we calculate a residence time for seawater sulfate of ~55 kyrs, which is an order of magnitude longer than the modern ocean mixing time (~3 kyrs). Relative

690 homogeneity in Aptian $\delta^{34}S_{CAS}$ records is thus expected, even with seawater
691 sulfate concentrations well below 1 mM.
692
693 **5.0 Implications and conclusions**
694 At 28 mM, seawater sulfate is an oxidant pool twice the size of modern
695 atmospheric O_2. A decline to below 300 µM seawater sulfate concentrations
696 consequently indicates a large-scale reorganization of global oxidant pools during
697 OAE1a with implications for marine ecology, biogeochemical cycling, and climate.
698 Water column anoxia, for example, may have extended at least transiently into the
699 photic zone during OAE1a with potential to influence photosynthetic ecology.
700 Indeed, biomarkers indicative of green S-bacteria (phylum Chlorobi) have been
701 recovered in sediments deposited during OAE1a (van Breugel et al., 2007).
702 Preservation of biomarkers from green S-bacteria in Aptian ferruginous sediments
703 could signal the return of photoferrotrophy to the Phanerozoic oceans, as they are
704 known to grow on ferrous Fe (photoferrotrophy) (Crowe et al., 2008). Low-sulfate,
705 ferruginous oceans would also have channelled OM degradation from sulfate
706 reduction to methanogenesis and limited the consumption of this methane through
707 anaerobic oxidation with sulfate (Reeburgh, 2007). Seawater sulfate
708 concentrations <300 µM could thus promote marine methane efflux to the
709 atmosphere with potential greenhouse warming.
710 Development of ferruginous conditions during OAE1a reveals large-scale
711 dynamics in Earth's biogeochemical cycles over intervals of <100 kyrs. The
712 development of ferruginous ocean conditions during multiple OAEs may thus
713 signify a general instability in Earth surface redox budgets and the recurrent
714 reorganization of major oxidant pools at Earth's surface, like seawater sulfate,
715 during the Phanerozoic Eon. In particular, emerging reconstructions of seawater
716 sulfate concentrations during multiple Phanerozoic OAEs, suggest repeated
717 collapse of the seawater sulfate reservoir to below 1 mM, possibly below 100 µM,
718 over short timescales (<50 kyrs) (He et al., 2020). The mechanisms driving this
719 reorganization remain uncertain but could be addressed through better constraints
720 on global S-budgets and the drivers of ocean deoxygenation, as well as Earth

system modeling that resolves such biogeochemical dynamics over relatively short time scales.

Figures and captions

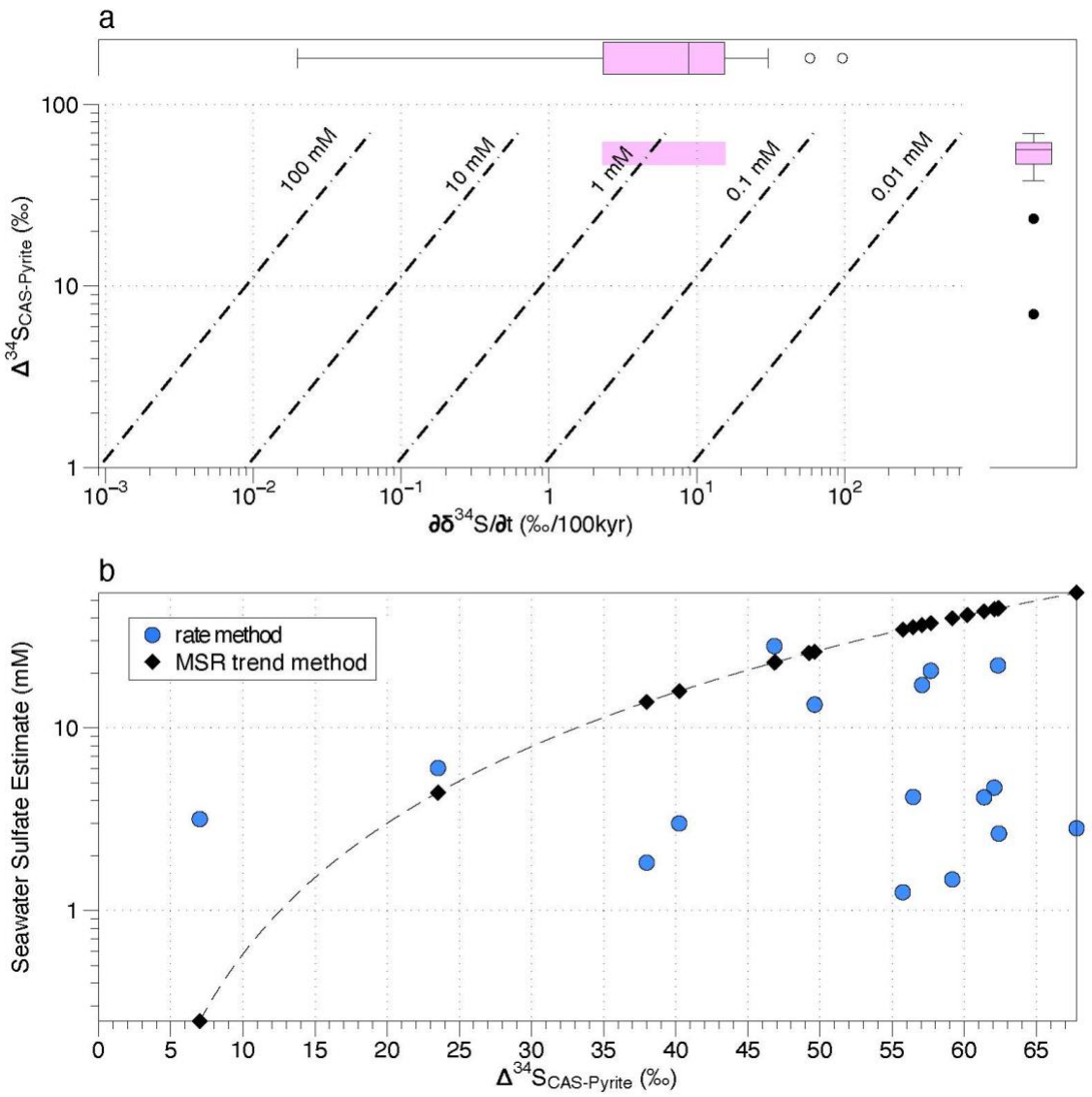

Figure 1. (a) Rate method estimates for early Aptian seawater sulfate concentrations using the approach presented in (Algeo et al., 2015). Seawater sulfate concentrations were calculated using a S-pyrite burial flux of 1.3 x 10^{12} mol yr^{-1}. The x-axis box and whisker plot represent $\partial \delta^{34}S_{CAS}/\partial t$ calculated using Aptian S-isotope data from (Gomes et al., 2016; Kristall et al., 2018; Mills et al., 2017). The y-axis box and whisker plot represents $\Delta^{34}S_{CAS\text{-}Pyrite}$ from (Gomes et al., 2016; Kristall et al., 2018; Mills et al., 2017) The pink shaded region represents the parameter space where the ranges between the 25th and 75th percentiles of the $\Delta^{34}S_{CAS}$ and $\partial \delta^{34}S_{CAS}/\partial t$ distributions overlap, corresponding to a likely range of range of seawater sulfate estimates. **(b)** All data points represent paired cogenetic S-isotope data for Aptian sulfate ($\delta^{34}S_{CAS}$) and sulfide ($\delta^{34}S_{Pyrite}$) (Gomes et al., 2016). For the rate method, seawater sulfate concentrations were calculated using a S-pyrite burial flux of 1.3 x 10^{12} mol yr^{-1}. For the MSR trend method, the values were calculated using the relationship presented in (Algeo et al., 2015) (Supplementary Information).

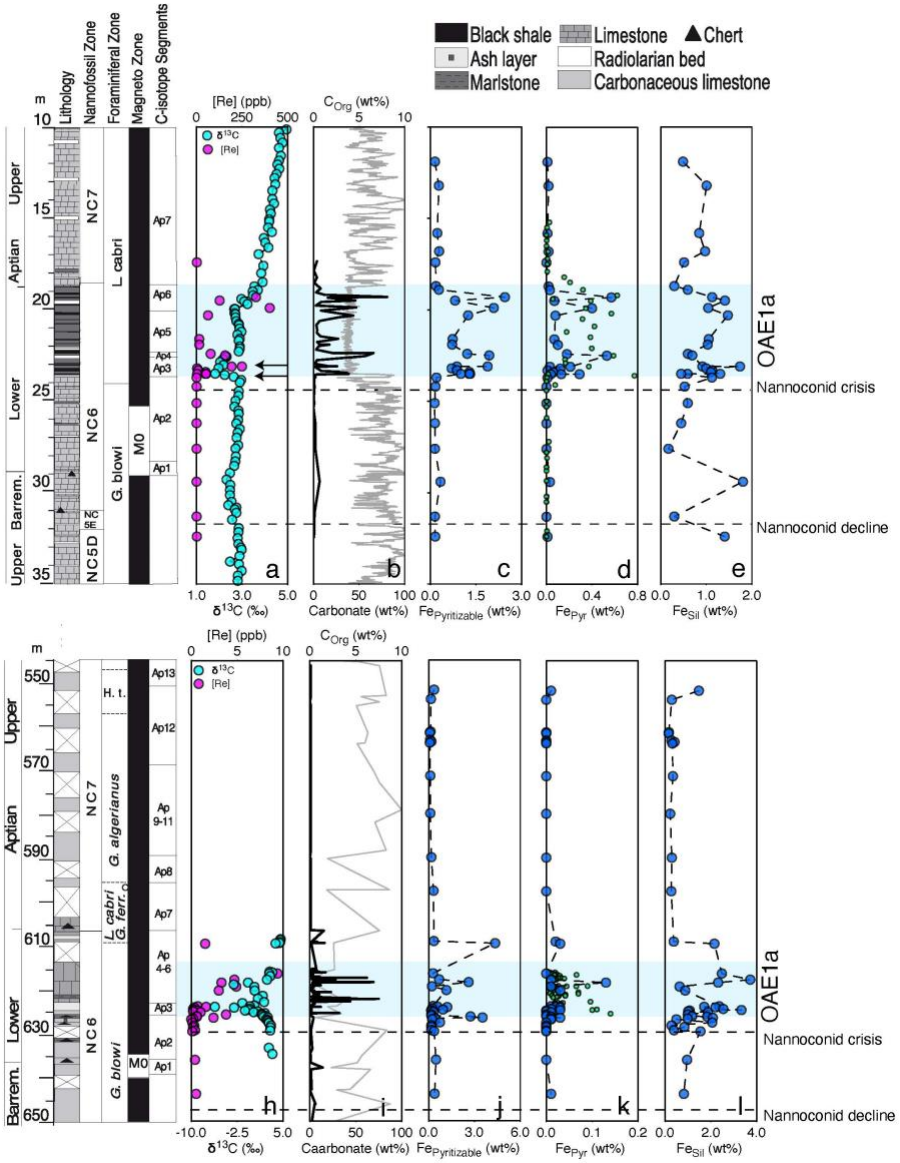

Figure 2. Fe-speciation and carbon isotope records for Cismon and DSDP Site 463 cores. Integrated stratigraphy of the Cismon and DSDP Site 463 after (Bottini et al., 2015; Erba et al., 2010). The grey shaded region (OAE1a) represents ~1.1 Myrs (Malinverno et al., 2010), C-isotope stages C2–C7 (Bottini et al., 2015). Panels (a-e) are Cismon data and panels (f-j) are DSDP Site 463 data. **(a)** Cismon C-isotope data from (Bottini et al., 2015). Rhenium concentration data from (Bottini et al., 2012). **(b)** Carbonate C, and organic matter C data after (Bottini et al., 2012; Bottini et al., 2015). (**c**) $Fe_{Pyritizable}$; sum of all pyritizable Fe_{HR} pools (Fe_{Carb}, Fe_{OM}, Fe_{Ox}) **(d)** Fe_{Sil}; silicate Fe **(e)** Fe_{Pyr}; pyrite Fe. Green data represent pyrite concentration data from (Gomes et al., 2016). **(f)** DSDP Site 463 C-isotope data from (Bottini et al., 2012). Rhenium concentration data from (Bottini et al., 2012). **(g)** Carbonate C data from (Bottini et al., 2015), organic C data from (Bottini et al., 2015; van Breugel et al., 2007). (**h)** $Fe_{Pyritizable}$; sum of all pyritizable Fe_{HR} pools (Fe_{Carb}, Fe_{OM}, Fe_{Ox}) **(i)** Fe_{Sil}; silicate Fe. **(j)** Fe_{Pyr}; pyrite Fe. Green data represent pyrite concentration estimates from (Mélières et al., 1981). The start of the nannoconid decline and beginning of the nannoconid crisis are marked with dashed lines (Erba et al., 2010).

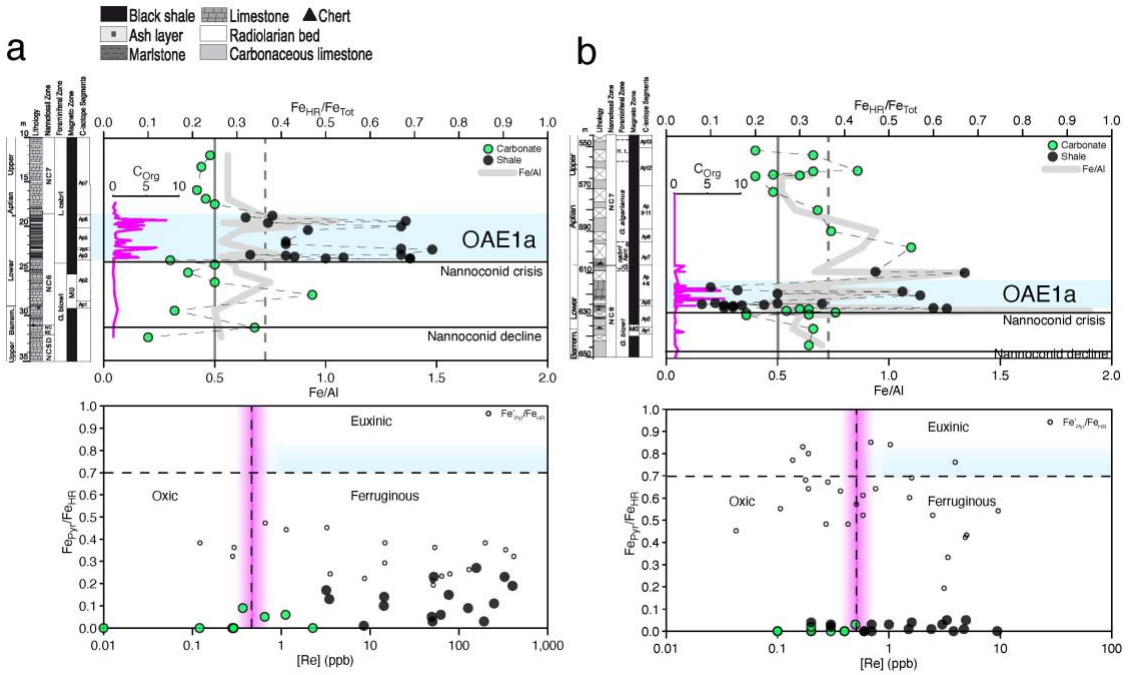

Figure 3. (a) Fe-speciation and Fe/Al records of the Cismon and DSDP Site 463 **(b)**. The vertical and horizontal dotted lines refer to the oxic-anoxic threshold (Fe_{HR}/Fe_{Tot} = 0.38) and a conservative ferruginous-euxinic threshold (Fe_{Pyr}/Fe_{HR} = 0.70), respectively. The open circles represent Fe'_{Pyr}/Fe_{HR}, the amount of pyrite present in the samples assuming the unlikely scenario where the entire Fe_{Ox} pool is a result of Fe_{Pyr} oxidation. The solid vertical line in the top panels refers to the Fe/Al ratio of 0.5. The solid vertical line in the bottom panels refers to the average rhenium concentration of the PAAS, with the purple shading representing a 2 sigma uncertainty on this value (McLennan, 2001). Litho-, bio- and magneto-stratigraphy is the same as Figure 1.

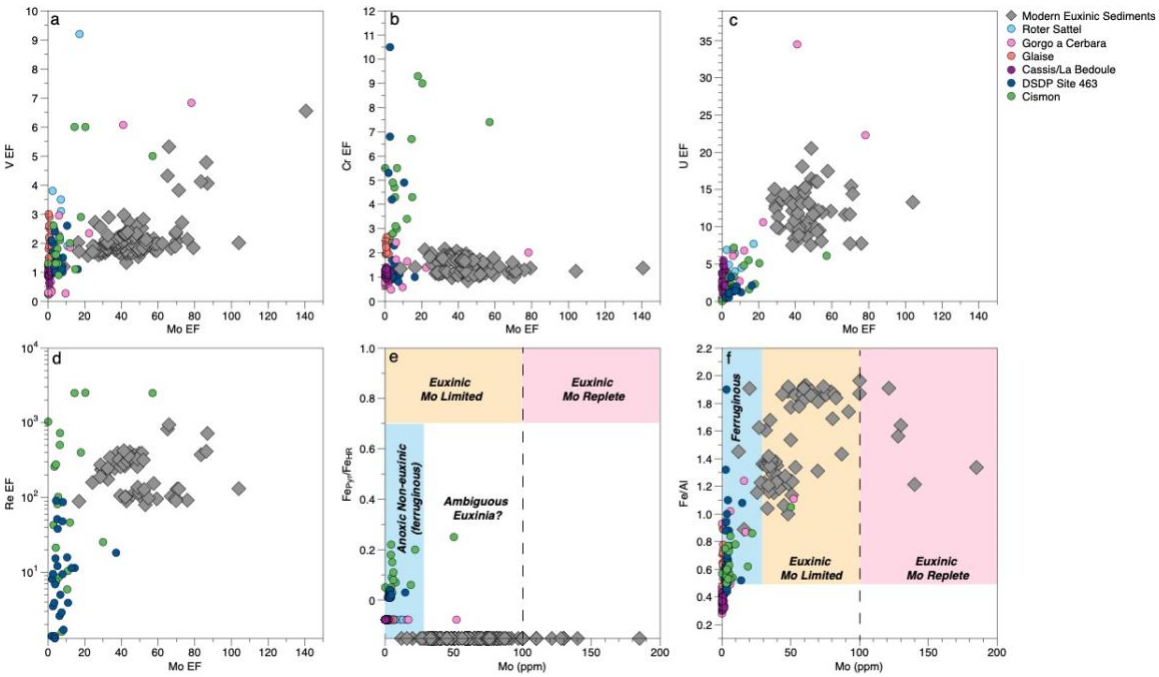

Figure 4. RSTE enrichment factors (EFs) and molybdenum concentrations. EFs were calculated by normalizing to the PAAS. Data from other OAE1a sedimentary sections as follows; Gorgo a Cerbara, Glaise, and Cassis la Bédoule (Follmi, 2012; Westermann et al., 2013), Roter Sattel (Charbonnier et al., 2018). All modern environment RSTE data come from hydrologically restricted euxinic basins (Bennett and Canfield, 2020). **(a)** V EFs vs Mo EFs. **(b)** Cr EFs vs. Mo EFs. **(c)** U EFs vs. Mo EFs. **(d)** Re EFs vs. Mo EFs. **(e)** Fe_{Pyr}/Fe_{HR} vs. Mo concentrations. The data for other OAE1a sections and modern environments do not have corresponding Fe_{Pyr} values and thus these data plot on the x-axis. All OAE1a data points (2 analyses excepted) exhibit Mo concentrations that unambiguously demonstrate non-euxinic conditions. **(f)** Fe/Al vs. Mo concentrations. Fe/Al ratios >0.5 imply anoxic conditions (Lyons and Severmann, 2006). All OAE1a data points that plot above this threshold (2 analyses excepted) exhibit Mo concentrations that unambiguously demonstrate ferruginous (non-euxinic) conditions.

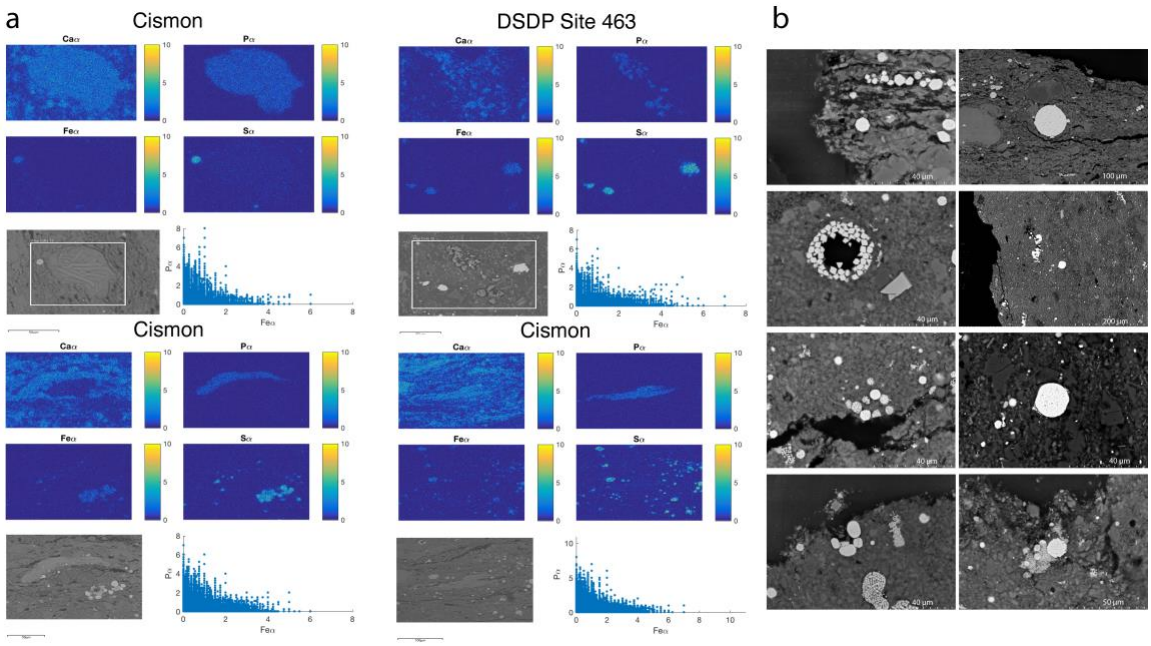

Figure 5. (a) SEM-EDS analyses of Ca-P bearing minerals (apatite) in the Cismon and DSDP Site 463 sediments. We observe a tight coupling between the distribution of Ca and P in the OAE1a samples, and no relationship between the distribution of Fe and P, implying no redistribution of P into freshly formed poorly crystalline Fe-(oxyhydr)oxide phases and a lack of the pyrite oxidation mechanism observed by Kraal et al. (2009). **(b)** Compilation of back scatter electron (BSE) SEM images obtained on thin sections of OAE1a samples from both the Cismon and DSDP Site 463 sediments. We observe no strong evidence for pyrite oxidation, even on crystals located near thin section boundaries where oxidation would be most concentrated.

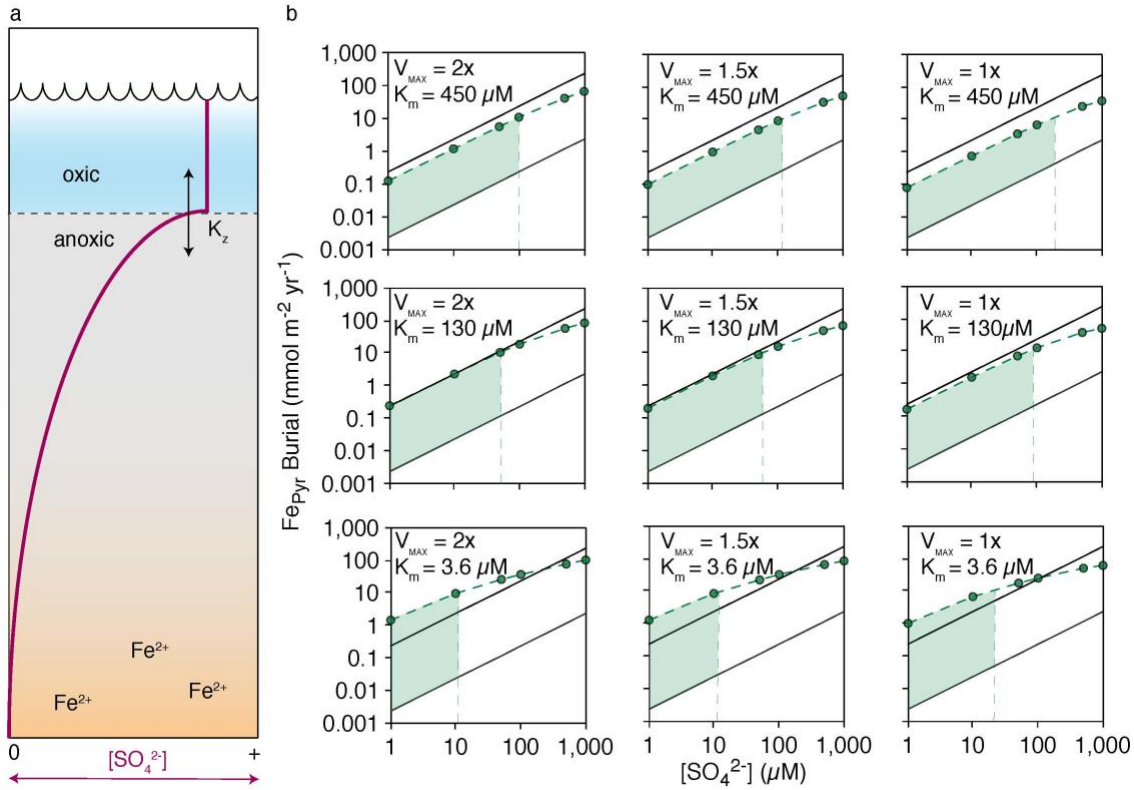

Figure 6. 1D water column reaction transport model sensitivity analyses. **(a)** Schematic model representation of a stratified Cretaceous water column. The model is designed such that seawater sulfate must be exhausted by the bottom of the domain (sediment-water interface) under anoxic conditions via sulfate reduction promoting the development of ferruginous conditions. **(b)** Water column depth integrated sulfate reduction rates (equivalent to pyrite burial). The data points represent different model outputs for the indicated scenarios. The solid black lines (equation = $[SO_4^{2-}]/\partial z * K_z$) mark the pyrite burial rates needed to support complete drawdown of sulfate at a given surface seawater sulfate concentration. The lower line corresponds to a K_z = 0.01 m^2 d^{-1} and the upper line corresponds to a K_z of 1 m^2 d^{-1}. The only allowable model runs thus need to plot above these lines. The green shading corresponds to the allowable parameter space that satisfies both the requirement for complete sulfate drawdown and the conservative condition for local pyrite burial rates to be less than 10 mmol m^2 yr^{-1} (Fig. S6). Maximum allowable sulfate concentrations come from the intersection of the green shading (extended green dashed lines) with the x-axis.

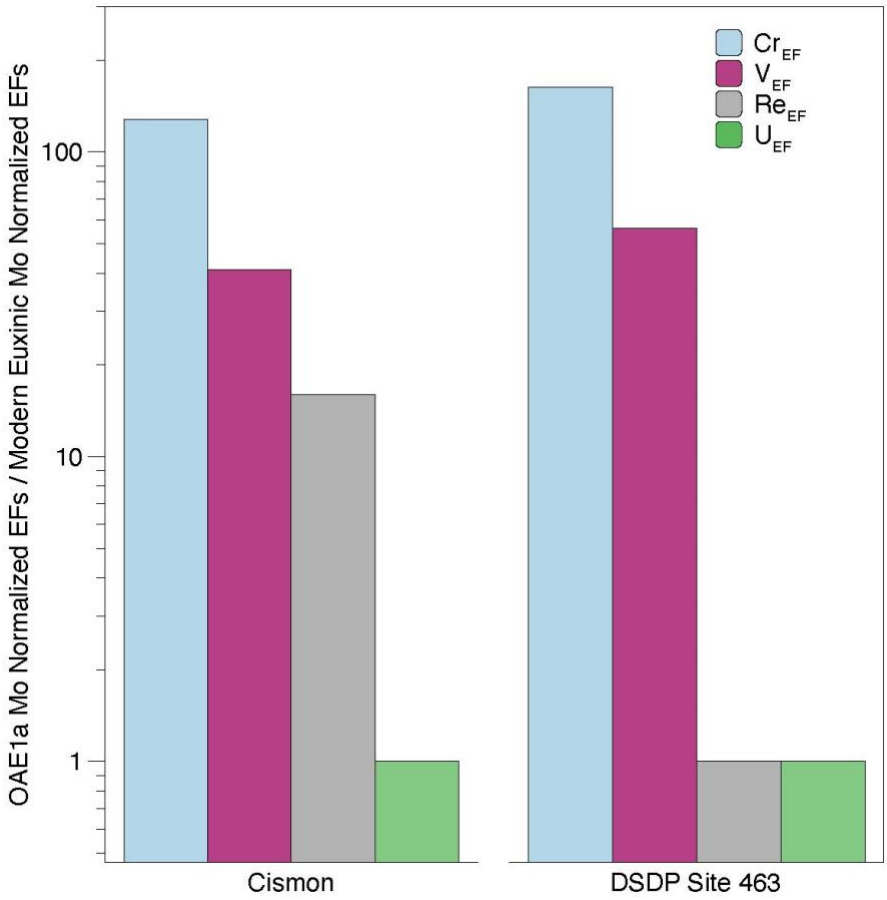

Figure 7. OAE1a RSTE enrichment factors (EFs) compared to modern euxinic sediments. Displayed are EFs of RSTEs normalized to Mo enrichment factor in the OAE1a sediments compared to RSTE EFs normalized to Mo in example modern euxinic basins; $\frac{(OAE1a \frac{RSTE_{EF}}{Mo_{EF}})}{(Modern\ Euxinic \frac{RSTE_{EF}}{Mo_{EF}})}$. We find that the RSTE enrichment factors of Cr, V, and Re, metals that do not require sulfide to be buried under anoxic conditions, are dramatically enriched in both the Cismon and DSDP 463 sediments, relative to modern euxinic basins. Modern data is from (Bennett and Canfield, 2020).

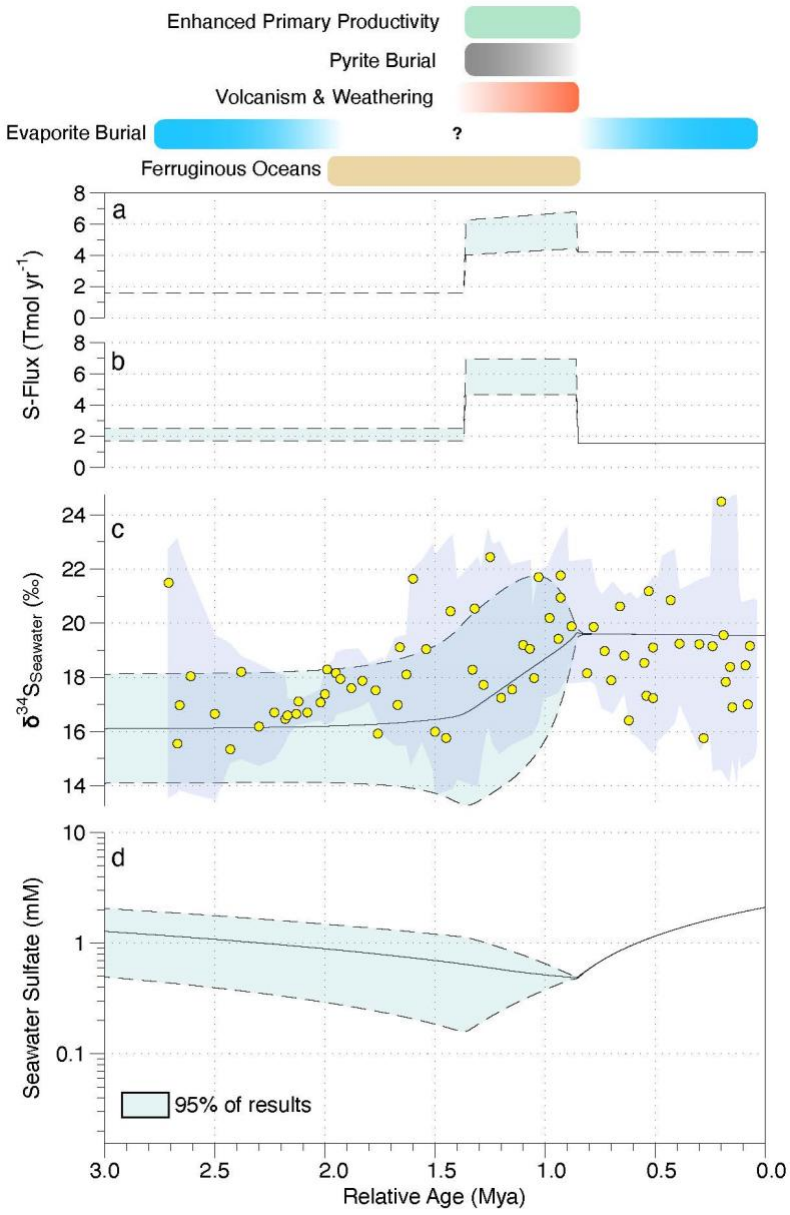

Figure 8. Evolution of the Cretaceous seawater sulfate reservoir. The coloured bars represent the conceptual model and proposed timing of early Cretaceous events associated with the development of OAE1a. **(a)** Modelled S-input and **(b)** burial fluxes. Solid lines represent the mean results of the stochastic modeling (Supplementary Information), whereas the shaded region between the dashed lines encompasses 95% of the results. **(c)** Modelled $\delta^{34}S_{sulfate}$. Solid lines represent the mean results of the stochastic modeling (Supplementary Information), whereas the shaded region between the dashed lines encompasses 95% of the results. The yellow data points represent Aptian $\delta^{34}S_{CAS}$ data from (Gomes et al., 2016; Kristall et al., 2018; Mills et al., 2017). The purple shading represents a 5-point $\delta^{34}S_{CAS}$ moving average of the S-isotope data using a 2s.d. error envelope. **(d)** Modeled seawater sulfate concentrations. Solid lines represent the mean results of the stochastic modeling (Supplementary Information), whereas the shaded region between the dashed lines encompasses 95% of the results.

Acknowledgements

This work was funded through NSERC Discovery Grants to Sean A. Crowe (0487) and Roger Francois, the Canadian Foundation for Innovation, the Canada Research Chairs Program, and a UBC 4-Year Fellowship to Kohen W. Bauer. EE and CB were funded by PRIN 2017RX9XXY to EE. We thank the International Ocean Discovery Program (IODP) for providing the DSDP Site 463 samples. We thank John Greenough for help with the milling of rock samples. We also acknowledge Steve Calvert for participating in helpful discussions on rhenium geochemistry.

Data availability statement

The datasets and models generated during and/or analysed during the current study are available from the corresponding author on reasonable request.

CRediT author statement

KWB: validation, formal analysis, investigation, data curation, writing, visualization. **CB**: resources, data curation, visualization, validation, writing. **SK**: validation, software, methodology, formal analysis, writing. **MJ**: validation, writing. **RF**: conceptualization, validation, supervision, funding acquisition, writing. **EE**: resources, visualization, validation, writing. **SAC**: conceptualization, validation, supervision, project administration, funding acquisition, writing.

References

Algeo, T.J., Luo, G.M., Song, H.Y., Lyons, T.W., Canfield, D.E., 2015. Reconstruction of secular variation in seawater sulfate concentrations. Biogeosciences 12, 2131-2151.

Bennett, W.W., Canfield, D.E., 2020. Redox-sensitive trace metals as paleoredox proxies: A review and analysis of data from modern sediments. Earth-Sci. Rev. 204.

Berner, R.A., 1981. A new geochemical classification of sedimentary environments. Journal of Sedimentary Research 51, 359-365.

Bottini, C., Cohen, A.S., Erba, E., Jenkyns, H.C., Coe, A.L., 2012. Osmium-isotope evidence for volcanism, weathering, and ocean mixing during the early Aptian OAE 1a. Geology 40, 583-586.

Bottini, C., Erba, E., Tiraboschi, D., Jenkyns, H., Schouten, S., Sinninghe Damsté, J., 2015. Climate variability and ocean fertility during the Aptian Stage. Climate of the Past 11, 383-402.

Canfield, D.E., Farquhar, J., 2012. The global sulfur cycle. Fundamentals of geobiology, 49-64.

Chaboureau, A.C., Guillocheau, F., Robin, C., Rohais, S., Moulin, M., Aslanian, D., 2013. Paleogeographic evolution of the central segment of the South Atlantic during Early Cretaceous times: Paleotopographic and geodynamic implications. Tectonophysics 604, 191-223.

Charbonnier, G., Adatte, T., Spangenberg, J.E., Follmi, K.B., 2018. The expression of early Aptian to latest Cenomanian oceanic anoxic events in the sedimentary record of the Brianconnais domain. Global and Planetary Change 170, 76-92.
Chen, C.T.A., Lin, C.M., Huang, B.T., Chang, L.F., 1996. Stoichiometry of carbon, hydrogen, nitrogen, sulfur and oxygen in the particulate matter of the western North Pacific marginal seas. Marine Chemistry 54, 179-190.
Crowe, S.A., Jones, C., Katsev, S., Magen, C., O'Neill, A.H., Sturm, A., Canfield, D.E., Haffner, G.D., Mucci, A., Sundby, B., Fowle, D.A., 2008. Photoferrotrophs thrive in an Archean Ocean analogue. Proceedings of the National Academy of Sciences of the United States of America 105, 15938-15943.
Crowe, S.A., Paris, G., Katsev, S., Jones, C., Kim, S.-T., Zerkle, A.L., Nomosatryo, S., Fowle, D.A., Adkins, J.F., Sessions, A.L., Farquhar, J., Canfield, D.E., 2014. Sulfate was a trace constituent of Archean seawater. Science 346, 735-739.
Davison, I., 2007. Geology and tectonics of the South Atlantic Brazilian salt basins. Geological Society, London, Special Publications 272, 345-359.
Erba, E., Bottini, C., Weissert, H.J., Keller, C.E., 2010. Calcareous Nannoplankton Response to Surface-Water Acidification Around Oceanic Anoxic Event 1a. Science 329, 428-432.
Fagerbakke, K.M., Heldal, M., Norland, S., 1996. Content of carbon, nitrogen, oxygen, sulfur and phosphorus in native aquatic and cultured bacteria. Aquatic Microbial Ecology 10, 15-27.
Follmi, K.B., 2012. Early Cretaceous life, climate and anoxia. Cretaceous Research 35, 230-257.
Gomes, M.L., Hurtgen, M.T., Sageman, B.B., 2016. Biogeochemical sulfur cycling during Cretaceous oceanic anoxic events: A comparison of OAE1a and OAE2. Paleoceanography 31, 233-251.
Hardisty, D.S., Lyons, T.W., Riedinger, N., Isson, T.T., Owens, J.D., Aller, R.C., Rye, D.M., Planavsky, N.J., Reinhard, C.T., Gill, B.C., 2018. An evaluation of sedimentary molybdenum and iron as proxies for pore fluid paleoredox conditions. Am. J. Sci. 318, 527-556.
Hartnett, H.E., Devol, A.H., 2003. Role of a strong oxygen-deficient zone in the preservation and degradation of organic matter: A carbon budget for the continental margins of northwest Mexico and Washington State. Geochimica Et Cosmochimica Acta 67, 247-264.
He, T., Dal Corso, J., Newton, R.J., Wignall, P.B., Mills, B.J., Todaro, S., Di Stefano, P., Turner, E.C., Jamieson, R.A., Randazzo, V., 2020. An enormous sulfur isotope excursion indicates marine anoxia during the end-Triassic mass extinction. Science Advances 6, eabb6704.
Horner, T.J., Pryer, H.V., Nielsen, S.G., Crockford, P.W., Gauglitz, J.M., Wing, B.A., Ricketts, R.D., 2017. Pelagic barite precipitation at micromolar ambient sulfate. Nature Communications 8.
Jellinek, A., Lenardic, A., Pierrehumbert, R., 2020. Ice, fire, or fizzle: The climate footprint of Earth's supercontinental cycles. Geochemistry, Geophysics, Geosystems 21, e2019GC008464.
Jenkyns, H.C., 2010. Geochemistry of oceanic anoxic events. Geochemistry Geophysics Geosystems 11, 30.

1005 Kraal, P., Slomp, C.P., Forster, A., Kuypers, M.M.M., Sluijs, A., 2009. Pyrite oxidation
1006 during sample storage determines phosphorus fractionation in carbonate-poor
1007 anoxic sediments. Geochimica Et Cosmochimica Acta 73, 3277-3290.
1008 Kristall, B., Jacobson, A.D., Sageman, B.B., Hurtgen, M.T., 2018. Coupled strontium-
1009 sulfur cycle modeling and the Early Cretaceous sulfur isotope record.
1010 Palaeogeography Palaeoclimatology Palaeoecology 496, 305-322.
1011 Luther III, G.W., Giblin, A., Howarth, R.W., Ryans, R.A., 1982. Pyrite and oxidized iron
1012 mineral phases formed from pyrite oxidation in salt marsh and estuarine sediments.
1013 Geochimica et Cosmochimica Acta 46, 2665-2669.
1014 Lyons, T.W., Severmann, S., 2006. A critical look at iron paleoredox proxies: New
1015 insights from modern euxinic marine basins. Geochimica Et Cosmochimica Acta 70,
1016 5698-5722.
1017 Malinverno, A., Erba, E., Herbert, T.D., 2010. Orbital tuning as an inverse problem:
1018 Chronology of the early Aptian oceanic anoxic event 1a (Selli Level) in the Cismon
1019 APTICORE. Paleoceanography 25.
1020 Martin, J.H., Knauer, G.A., Karl, D.M., Broenkow, W.W., 1987. VERTEX: carbon cycling
1021 in the northeast Pacific. Deep Sea Research Part A. Oceanographic Research Papers
1022 34, 267-285.
1023 Marz, C., Poulton, S.W., Beckmann, B., Kuster, K., Wagner, T., Kasten, S., 2008. Redox
1024 sensitivity of P cycling during marine black shale formation: Dynamics of sulfidic
1025 and anoxic, non-sulfidic bottom waters. Geochimica Et Cosmochimica Acta 72, 3703-
1026 3717.
1027 McAnena, A., 2011. The reactivity and isotopic fractionation of Fe-bearing minerals
1028 during sulfidation: an experimental approach. Newcastle University.
1029 McLennan, S.M., 2001. Relationships between the trace element composition of
1030 sedimentary rocks and upper continental crust. Geochemistry Geophysics
1031 Geosystems 2, art. no.-2000GC000109.
1032 Mélières, F., Deroo, G., Herbin, J.-P., 1981. Organic-matter-rich and hypersiliceous
1033 Aptian sediments from Western Mid-Pacific Mountains, Deep Sea Drilling Project
1034 Leg 62, Initial Reports of the Deep Sea Drilling Project. U.S. Govt. Printing Office.
1035 Mills, J.V., Gomes, M.L., Kristall, B., Sageman, B.B., Jacobson, A.D., Hurtgen, M.T., 2017.
1036 Massive volcanism, evaporite deposition, and the chemical evolution of the Early
1037 Cretaceous ocean. Geology 45, 475-478.
1038 Munk, W., Wunsch, C., 1998. Abyssal recipes II: Energetics of tidal and wind mixing.
1039 Deep Sea Research Part I: Oceanographic Research Papers 45, 1977-2010.
1040 Olson, S.L., Reinhard, C.T., Lyons, T.W., 2016. Limited role for methane in the mid-
1041 Proterozoic greenhouse. Proceedings of the National Academy of Sciences of the
1042 United States of America 113, 11447-11452.
1043 Paris, G., Adkins, J.F., Sessions, A.L., Webb, S.M., Fischer, W.W., 2014. Neoarchean
1044 carbonate-associated sulfate records positive Delta S-33 anomalies. Science 346,
1045 739-741.
1046 Poulton, S.W., Canfield, D.E., 2005. Development of a sequential extraction
1047 procedure for iron: implications for iron partitioning in continentally derived
1048 particulates. Chemical Geology 214, 209-221.
1049 Poulton, S.W., Canfield, D.E., 2006. Co-diagenesis of iron and phosphorus in
1050 hydrothermal sediments from the southern East Pacific Rise: Implications for the

evaluation of paleoseawater phosphate concentrations. Geochimica Et Cosmochimica Acta 70, 5883-5898.
Poulton, S.W., Canfield, D.E., 2011. Ferruginous Conditions: A Dominant Feature of the Ocean through Earth's History. Elements 7, 107-112.
Poulton, S.W., Henkel, S., Marz, C., Urquhart, H., Flogel, S., Kasten, S., Damste, J.S.S., Wagner, T., 2015. A continental-weathering control on orbitally driven redox-nutrient cycling during Cretaceous Oceanic Anoxic Event 2. Geology 43, 963-966.
Raiswell, R., Hardisty, D.S., Lyons, T.W., Canfield, D.E., Owens, J.D., Planavsky, N.J., Poulton, S.W., Reinhard, C.T., 2018. The iron paleoredox proxies: A guide to the pitfalls, problems and proper practice. Am. J. Sci. 318, 491-526.
Reeburgh, W.S., 2007. Oceanic methane biogeochemistry. Chemical Reviews 107, 486-513.
Stolper, D.A., Keller, C.B., 2018. A record of deep-ocean dissolved O2 from the oxidation state of iron in submarine basalts. Nature 553, 323-327.
Tedeschi, L.R., Jenkyns, H.C., Robinson, S.A., Sanjines, A.E.S., Viviers, M.C., Quintaes, C., Vazquez, J.C., 2017. New age constraints on Aptian evaporites and carbonates from the South Atlantic: Implications for Oceanic Anoxic Event 1a. Geology 45, 543-546.
Timofeeff, M.N., Lowenstein, T.K., da Silva, M.A., Harris, N.B., 2006. Secular variation in the major-ion chemistry of seawater: Evidence from fluid inclusions in Cretaceous halites. Geochimica Et Cosmochimica Acta 70.
Tribovillard, N., Algeo, T.J., Lyons, T., Riboulleau, A., 2006. Trace metals as paleoredox and paleoproductivity proxies: an update. Chemical geology 232, 12-32.
van Breugel, Y., Schouten, S., Tsikos, H., Erba, E., Price, G.D., Damste, J.S.S., 2007. Synchronous negative carbon isotope shifts in marine and terrestrial biomarkers at the onset of the early Aptian oceanic anoxic event 1a: Evidence for the release of C-13-depleted carbon into the atmosphere. Paleoceanography 22.
Werne, J.P., Lyons, T.W., Hollander, D.J., Formolo, M.J., Damsté, J.S.S., 2003. Reduced sulfur in euxinic sediments of the Cariaco Basin: sulfur isotope constraints on organic sulfur formation. Chemical Geology 195, 159-179.
Westermann, S., Stein, M., Matera, V., Fiet, N., Fleitmann, D., Adatte, T., Foellmi, K.B., 2013. Rapid changes in the redox conditions of the western Tethys Ocean during the early Aptian oceanic anoxic event. Geochimica Et Cosmochimica Acta 121, 467-486.
Wortmann, U.G., Chernyavsky, B.M., 2007. Effect of evaporite deposition on Early Cretaceous carbon and sulphur cycling. Nature 446, 654-656.